PAPER

Check for updates

Effects of hydration water on bioresponsiveness of polymer interfaces revealed by analysis of linear and cyclic polymer-grafted substrates†

Shin-nosuke Nishimura, [ID] ‡[ad] Naoya Kurahashi,‡[bc] Shohei Shiomoto, [ID] ‡§[a] Yoshihisa Harada [ID] *[ce] and Masaru Tanaka [ID] *[a]

Given that the hydration water of polymer matrices may differ from that of outermost polymer surfaces, processes at biomaterial–biofluid interfaces and role of hydration water therein cannot be adequately examined using most conventional characterization methods. To bridge this gap, a gold substrate was herein modified with linear and cyclic poly(2-methoxyethyl acrylate) to prepare *gl*-PMEA and *gc*-PMEA surfaces, respectively, as models for the outermost surfaces of blood-contacting medical devices. Both surfaces suppressed the adhesion of human platelets but differed in the adhesion behaviors of normal and tumor cells despite having the same areal density of fixed-end units. The surfaces were analyzed using quartz crystal microbalance (QCM), frequency modulation atomic force microscopy (FM-AFM), and X-ray emission spectroscopy (XES) measurements under wet conditions to clarify the relationship between bioresponsivity and hydration water. QCM measurements provided evidence that both grafted-PMEA were hydrated. FM-AFM observations revealed that the swelling layer was thicker for *gc*-PMEA. To rationalize the differences in the surface hydration states, we performed XES measurements under conditions enabling control over the number of hydration water molecules. In the low-water-content region, hydrogen bonds or interactions between water molecules developed in the vicinity of *gl*-PMEA but not *gc*-PMEA. Thus, the initial hydration behavior of the *gc*-PMEA surface, which promoted intermediate water formation, was different from that of the *gl*-PMEA surface. The results suggested that the adjustment and optimization of the hydration state of outermost biomaterial surfaces enable the control of bioresponsivity, including the selective isolation of tumor cells.

Introduction

Biocompatible polymers find numerous medical applications, *e.g.*, scaffolds for regenerative medicines,[1–6] carriers for drug delivery systems,[7,8] and coatings for medical devices,[9–14] and

[a] *Institute for Materials Chemistry and Engineering, Kyushu University, 744 Motooka, Nishi-ku, Fukuoka 819-0395, Japan. E-mail: masaru_tanaka@ms.ifoc.kyushu-u.ac.jp*

[b] *Department of Materials Molecular Science, Institute for Molecular Science, 38 Nishigonaka, Myodaijicho, Okazaki, Aichi 444-8585, Japan*

[c] *Institute for Solid State Physics, The University of Tokyo, 5-1-5 Kashiwanoha, Kashiwa, Chiba 277-8581, Japan. E-mail: harada@issp.u-tokyo.ac.jp*

[d] *Department of Molecular Chemistry and Biochemistry, Faculty of Science and Engineering, Doshisha University, 1-3 Tatara Miyakodani, Kyotanabe, Kyoto 610-0394, Japan*

[e] *Synchrotron Radiation Collaborative Research Organization, The University of Tokyo, 468-1 Aoba, Aramaki, Aoba-ku, Sendai, Miyagi 980-8572, Japan*

† Electronic supplementary information (ESI) available. See DOI: https://doi.org/10.1039/d4sm00977k

‡ S.N., N.K., and S.S. contributed equally to this paper.

§ Present address: Department of Materials Science and Technology, Faculty of Advanced Engineering, Tokyo University of Science, 6-3-1 Niijyuku, Katsushika, Tokyo 125-8585, Japan.

typically exhibit stealth properties while maintaining appropriate interactivity with the environment to prevent the undesirable activation of the biophylactic system without compromising biological function control. Purposeful biomaterial design requires the establishment of correlations between biomaterial properties and bioresponses, as exemplified by the effects of scaffold properties, such as surface roughness,[15–20] wettability,[20–23] and elastic modulus,[10,24–30] on cell adhesion, proliferation, and differentiation. However, these factors cannot comprehensively explain the observed bioresponses. Given that the phenomena occurring at the biomaterial–biofluid interface are not unique and should be essentially identical to other natural processes, bioresponses may be largely determined by a common factor, namely the hydration environment. Water, common and familiar to all organisms, forms a three-dimensional network through hydrogen bonding and therefore exhibits properties (*e.g.*, isobaric heat capacity, isothermal compressibility, and coefficient of thermal expansion) anomalous compared with those of typical liquids.[31]

Biomaterials are typically exposed to aqueous environments and, similar to biomolecules, feature surfaces that are always

hydrated. Hydration water at the biomaterial–biofluid interface is classified into three types of water: non-freezing water (NFW)/tightly bound water, intermediate water (IW)/loosely bound water, and free water (FW)/scarcely bound water, which plays distinct roles in determining bioresponses.[13,14,32,33] Previously, we showed that hydration water, especially IW, is closely related to the biocompatibility of biomaterial surfaces and cell behavior thereon.[34–37] Synthetic polymers capable of forming IW, e.g., poly(2-methoxyethyl acrylate) (PMEA) and its derivatives, are completely immune to platelet adhesion,[10,38–41] whereas the adhesion of normal and tumor cells depends on the IW amount.[42] Interestingly, IW formation strengthens cancer cell–polymer interactions.[43–45] Thus, hydration water control based on the rational design of the polymer structure may provide access to a new class of biomaterials.

For bulk polymer matrices, hydration water can be analyzed by differential scanning calorimetry (DSC),[32,46–48] infrared spectroscopy,[49,50] and nuclear magnetic resonance spectroscopy.[51] Although the results of these analyses are often well correlated with bioresponses, exceptions abound, possibly because the hydration water of polymer matrices may differ from that of outermost polymer surfaces. For example, neutron reflectometry measurements demonstrated that the water content of linear PMEA (l-PMEA) on the outermost surface ($\sim$40 wt%) exceeds that in the bulk state ($\sim$9 wt%).[52] Thus, an understanding of outermost-surface hydration water is needed to determine the major factors influencing material bioresponses. Quartz crystal microbalance (QCM) measurements,[53,54] atomic force microscopy (AFM),[54,55] and high-resolution X-ray emission spectroscopy (XES),[54] used to quantify surface water molecules, visualize surface morphology, and reveal the local hydrogen-bonded configurations of water molecules, respectively, are powerful tools for investigating the hydration behavior of the outermost surfaces of PMEA- and poly(n-butyl acrylate)-grafted substrates.

The bioresponses of cyclic polymers differ from those of linear polymers, e.g., cyclic PMEA (c-PMEA) forms a larger amount of IW than linear PMEA (l-PMEA) despite having the same primary structure.[56] Thus, c-PMEA- and l-PMEA-grafted substrates (gl- and gc-PMEA surfaces, respectively) enable the quantitative comparison of the outermost surfaces and their hydration states and the analysis of the corresponding differences. Herein, the outermost surfaces of blood-contacting medical devices were modeled using gl- and gc-PMEA surfaces to deepen our understanding of hydration water–bioresponse correlations. Specifically, we performed cell adhesion experiments using normal and tumor cells, analyzed surface hydration states using frequency modulation (FM-)AFM, QCM measurements, and XES, and discussed hydration water–bioresponse correlations.

Results and discussion

Preparation of gl- and gc-PMEA surfaces

The gl-PMEA (Fig. 1A) and gc-PMEA (Fig. 1B) surfaces were prepared by grafting thiol-terminated l-PMEA (M_n = 38 000; Đ = 1.17)[54] and disulfide-containing c-PMEA (M_n = 75 900;

Đ = 1.09),[56] respectively, on gold under the conditions listed in Table S1 (ESI†). The chain length of c-PMEA was almost twice that of l-PMEA, i.e., the lengths of the chains extending from the gold surface were almost identical, as were the areal densities of fixed MEA ends (Fig. 1C). The grafting density (σ) determined by QCM measurements (Table S2, ESI†). From the frequency changes of QCM substrates before and after grafting the polymers under air condition ($\Delta F_{grafted,air}$), the σ values of gl-PMEA and gc-PMEA were estimated to be 0.1 and 0.05 chain per nm^2, respectively. Note that the σ values of gl-PMEA was two times that of gc-PMEA because of the two-fold lower molecular weight of the former polymer. The gl-PMEA surface was reported to exhibit several advantages, such as the suppression of protein adsorption and platelet adhesion, as well as the physical coating system of l-PMEA, which is often used for extracorporeal membrane oxygenation (ECMO) devices and cardiopulmonary bypass circuits.[9] Although the gc-PMEA surface could have been prepared using a dithiol-type polymer (Fig. S1A, ESI†), this approach was expected to generate dangling SH groups and afford a nonuniformly grafted surface because of the variation in the distance between the fixed ends. Consequently, to obtain a uniformly grafted surface, we used a disulfide bond–containing precycled polymer (Fig. S1B, ESI†), as disulfide bonds are readily cleaved on gold surfaces to form Au–S bonds.[57]

The contact angles of bare gold, gl-PMEA, and gc-PMEA surfaces measured after 30 s drop adhesion (sessile drop method)/1 h soaking in water (captive bubble method) were 81.6 ± 1.2°/135.3 ± 0.4°, 63.5 ± 1.4°/140.9 ± 1.3°, and 78.5 ± 1.8°/142.5 ± 1.2°, respectively, confirming the successful grafting of l- and c-PMEA. Interestingly, the contact angles of the gc-PMEA surface determined by sessile drop and captive bubble methods were greater and lower than those of the gl-PMEA surface, respectively. The water droplet on the gc-PMEA surface (78.5 ± 1.8°) spread more slowly than that on the gl-PMEA
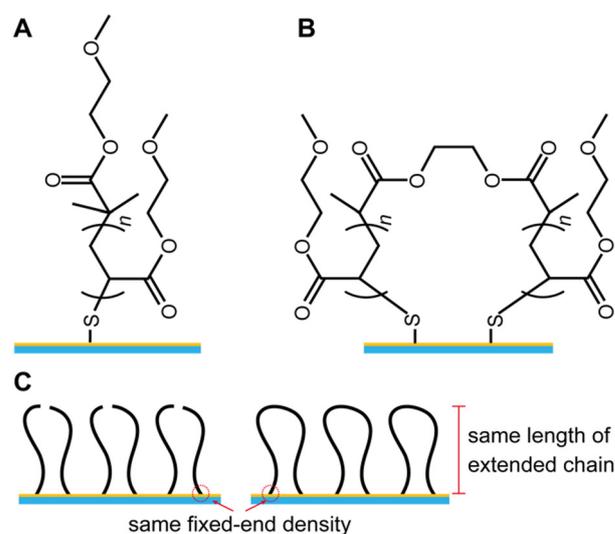

Fig. 1 Chemical structures of (A) linear poly(2-methoxyethyl acrylate)-grafted (gl-PMEA) and (B) cyclic poly(2-methoxyethyl acrylate)-grafted (gc-PMEA) surfaces and (C) corresponding conceptual illustration.

surface ($63.5 \pm 1.4°$), *i.e.*, the initial hydration was slower in the former case. Conversely, the air bubble contact angle of the *gc*-PMEA surface measured after soaking in water ($142.5 \pm 1.2°$) exceeded that of the *gl*-PMEA surface ($140.9 \pm 1.3°$), which suggested that the former surface was more hydrophilic and featured a larger amount of water. These findings agreed with the results of our previous work on bulk systems, namely with the fact that *c*-PMEA can contain a larger amount of water than *l*-PMEA despite featuring a lower water adsorption rate.[56] Thus, the present findings truly reflected the topology-related differences between the hydration ability/state of the *gl*-PMEA and *gc*-PMEA surfaces.

Fig. 2A shows the survey X-ray photoelectron spectra of bare gold, *gl*-PMEA, and *gc*-PMEA surfaces, revealing strong O 1s (534 eV) and C 1s (289 eV) signals and negligible Au-derived signals (4s: 763 eV, $4p_{1/2}$: 643 eV, $4p_{3/2}$: 547 eV, $4d_{3/2}$: 353 eV, $4d_{5/2}$: 335 eV, and 4f: 88 and 84 eV) after grafting. The O/C atomic ratio of the grafted surfaces ($\sim 1:2$) corresponded to that of PMEA. Most importantly, no sulfur signals were observed after grafting, which indicated the absence of dangling SH groups. PeakForce Tapping® (PFT)-mode AFM observations performed under dry conditions (Fig. 2B and C) showed that the *gl*-PMEA and *gc*-PMEA surfaces were extremely smooth (root mean square roughness (R_q) < 1 nm), confirming grafting uniformity and the absence of dangling SH groups. Thus, these surfaces were deemed suitable for evaluating bioresponses and elucidating the origins of the corresponding differences from the perspective of the hydration state (*i.e.*, NFW, IW, and FW).
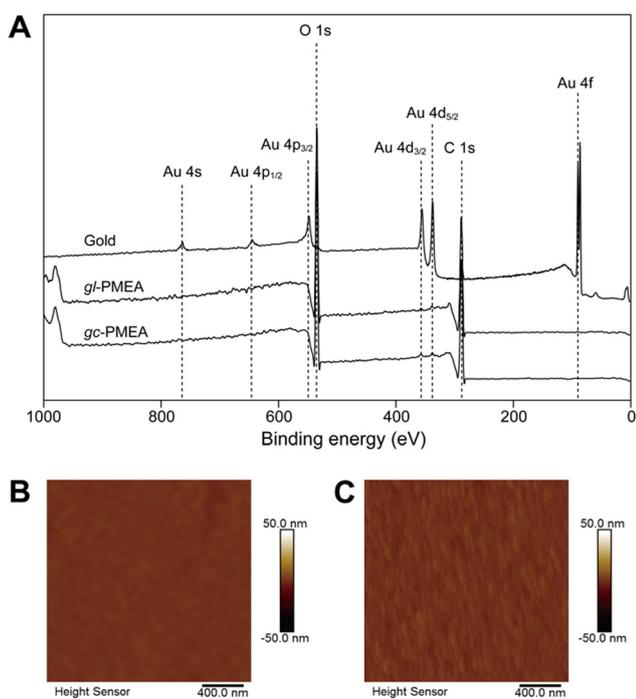
Bioresponses of PMEA-grafted surfaces

Platelet adhesion typically occurs within several minutes and is one of the most useful indicators of IW presence, as it is suppressed on surfaces with IW contents above a certain threshold.[33] Fig. 3A presents the results of human platelet adhesion tests. Numerous adhered platelets were observed (and activated) on the bare gold surface, whereas the *gl*-PMEA and *gc*-PMEA surfaces not only showed negligible platelet adhesion but also inhibited platelet activation, which indicated that a sufficient IW amount was formed by the surface PMEA chains. The number of adhered platelets on the *gc*-PMEA surface was significantly lower than that on the *gl*-PMEA surface. Given that platelet adhesion is progressively suppressed with an increasing amount of surface IW,[13,14,38] *gc*-PMEA formed IW more easily than *gl*-PMEA.

Fig. 3B presents the results of cell adhesion experiments. Given that the adhering cell type can be controlled by adjusting the IW amount,[42] we used normal human dermal fibroblasts (NHDFs) as normal cells, human breast tumor (MDA-MB-231) and cervical (HeLa) cells as epithelial cell adhesion molecule (EpCAM)-negative tumor cells, and human breast tumor (MCF-7)
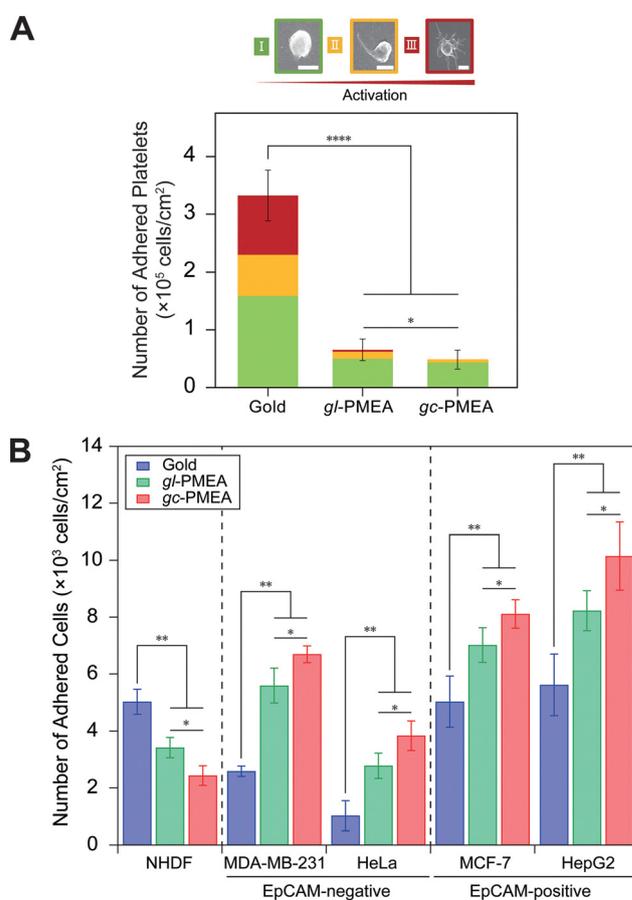

Fig. 3 (A) Results of human platelet adhesion tests, with the adherent platelets classified into types I (green), II (yellow), and III (red) based on their morphology. Scale bar is 2 μm. (B) Results of cell adhesion experiments. Error bars represent standard deviations. *p < 0.05, **p < 0.01, ****p < 0.001.

Fig. 2 (A) X-ray photoelectron spectra of the bare gold, *gl*-PMEA, and *gc*-PMEA surfaces. PeakForce Tapping® (PFT)-mode atomic force microscopy (AFM) images of the (B) *gl*-PMEA and (C) *gc*-PMEA surfaces acquired under dry conditions (scan area = 2 μm × 2 μm).

and hepatoma (HepG2) cells as EpCAM-positive tumor cells. EpCAM is a glycoprotein that functions as an epithelial cell adhesion molecule and is present in certain tumor cells. The normal and tumor cells (1.0×10^4 cells per cm^2) were seeded onto the surfaces and cultured at 37 °C for 6 h (the same time was used to examine initial cell adhesion). The number of NHDFs adhered to the bare gold surface exceeded that of NHDFs adhered to the polymer-grafted surfaces. In contrast, the EpCAM-negative and -positive tumor cells adhered to the polymer-grafted surfaces more readily than to the bare gold surface. These results well agreed with the fact that moderately IW-rich polymers prefer interacting with tumor cells rather than with normal cells,[42] implying that the presence of IW might promote tumor cell adhesion. Interestingly, compared with the *gl*-PMEA surface, the *gc*-PMEA surface suppressed the adherence of normal cells and promoted that of tumor cells. As mentioned above, the results of contact angle measurements suggested that the water content of the *gc*-PMEA surface exceeded that of the *gl*-PMEA surface. Thus, the unique hydration states of the polymer-grafted surfaces resulted in different bioresponses, although the effect of viscoelasticity due to water content differences cannot be excluded, demonstrating the great potential of hydration state-based surface design for the selective isolation of tumor cells.

Analyses of *gl*-PMEA and *gc*-PMEA hydration layers in water by AFM techniques

Cell responsiveness is affected by the characteristics of the outermost surfaces, such as the hydration layer of polymer interfaces, which consists of flexible polymers and water molecules.[58] As mentioned above, the *gl*-PMEA and *gc*-PMEA interfaces exhibited different cellular responses despite their identical extended-chain lengths and areal densities of MEA units. Shin *et al.* reported that the adsorption of biological fluids on a cyclic PEG–grafted interface was less pronounced than that on a linear PEG–grafted interface,[59] in line with the fact that the *gc*-PMEA interface suppressed platelet adhesion to a greater extent than the *gl*-PMEA interface. Previously, we demonstrated that bulk *l*-PMEA and *c*-PMEA have distinct hydration structures, *i.e.*, significantly differ in the amount of adsorbed water molecules and NFW : IW : FW ratio.[56] Hence, we hypothesized that the conformational differences between linear and cyclic polymers strongly influence the hydration structures of the bulk states and outermost interfaces of the grafting system, thus resulting in unique cell adhesion behaviors. The hydration state at the interface differs from that in the bulk, as demonstrated by Hirata *et al.*, who probed the *l*-PMEA/water interface by neutron reflectivity analysis and showed that the outermost layers had a considerably higher water content than the bulk interior.[60] However, no report has yet attempted to explain cell behavior by focusing on hydration at the outermost interface, which varies depending on the molecular conformation.

Hence, the hydrated layers of the *gl*-PMEA and *gc*-PMEA interfaces were herein observed using AFM to investigate their differences in swelling behaviors. Prior to these observations, we acquired the height profiles of the *gl*-PMEA and *gc*-PMEA interfaces in water by PFT-mode AFM to evaluate their submicron- or micron-scale structures in the *xy*-plane (Fig. 4A and C).

Both grafted PMEA interfaces were approximately flat, as revealed by their arithmetic averaged roughnesses, which equaled 0.39 and 0.76 nm for *gl*-PMEA and *gc*-PMEA, respectively, and were close to that of the bare gold substrate (0.51 nm) (Fig. S2A, ESI†). These results indicated that the gold interface was uniformly covered by *l*- and *c*-PMEA. A major difference was observed between the corresponding force mapping images, *i.e.*, the *xy*-directional
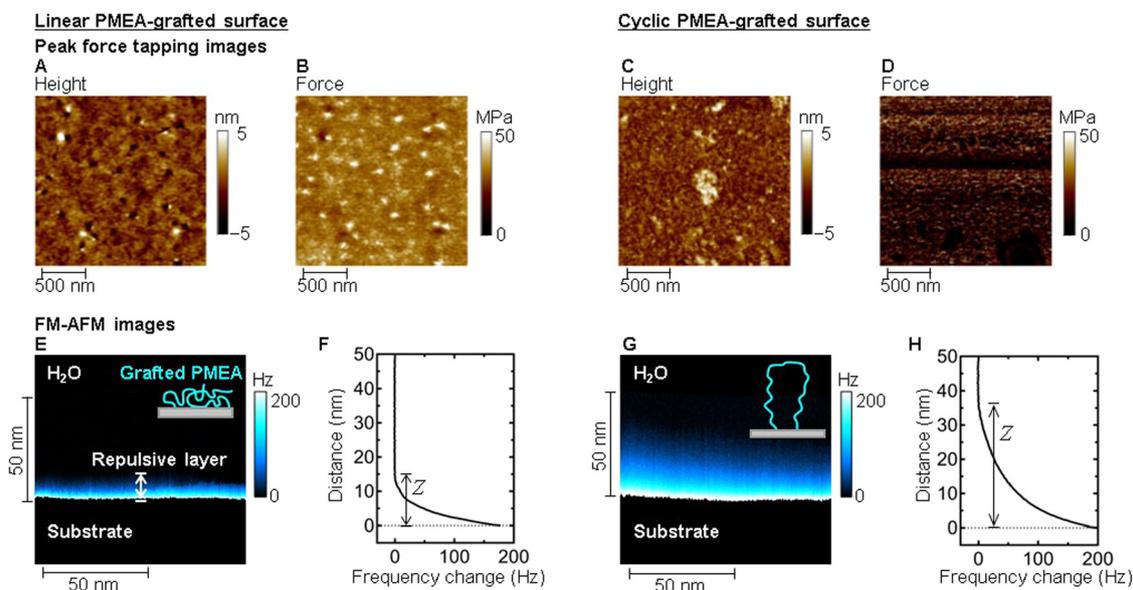

Fig. 4 Height (A) and (C) and force mapping (B) and (D) images (scan area = 2 μm × 2 μm) of (A) and (B) *gl*-PMEA and (C) and (D) *gc*-PMEA interfaces in water obtained using PFT-mode AFM. (E) and (G) *xz*-directional frequency modulation (FM)-AFM images (scan area = 100 nm × 50 nm) and (F) and (H) *z*-directional frequency curves of (E) and (F) *gl*-PMEA and (G) and (H) *gc*-PMEA interfaces in water.

stiffness distribution on the interface. The *gl*-PMEA (Fig. 4B) and *gc*-PMEA (Fig. 4D) interfaces showed stiffnesses of 33 and 7 MPa, respectively. Thus, compared with *gl*-PMEA, *gc*-PMEA formed a softer (more flexible) hydrated polymer layer with a greater water content.

We carried out QCM analyses to investigate swollen states of the polymer-grafts. The obtained frequency changes after hydration of the grafted polymer ($\Delta F_{grafted,water}$) were summarized in Table S2 (ESI†). The ratio of apparent hydrated mass to dry mass ($\Delta F_{grafted,water}/\Delta F_{grafted,air}$) were 1.50 ± 0.13 for *gl*-PMEA and 1.57 ± 0.05 for *gc*-PMEA, indicating the hydration of the polymer-grafts. However, comparison of these ratios should be avoided for discussion of the swollen states. The values of $\Delta F_{grafted,water}$ include the contribution of the molecular viscoelasticity, which is often affected by molecular conformation, diffusivity, and flexibility.[61,62]

Given that FM-AFM is a powerful tool for revealing the swollen states of the polymer layers at the nanoscale,[55] we acquired the *xz*-directional FM-AFM images of the *gl*- and *gc*-PMEA interfaces to compare the thicknesses of swollen PMEA layers. During imaging, the cantilever oscillated at the resonance frequency and was used for scanning in the surface-normal direction (*z*) at each horizontal (*x*) position. The change in the resonance frequency was due to the repulsive force arising from the excluded volume of the polymer chains and hydration water and therefore reflecting mass density. The intensity of the repulsive force was displayed using a color scale, with black meaning no force, cyan meaning medium force, and white meaning maximal force. The FM-AFM image of the *gl*-PMEA interface is shown in Fig. 4E. The black region on the upper side represents bulk water not interacting with the polymer chains. The band-shaped blue gradation indicates a repulsive layer due to the presence of hydrated *gl*-PMEA. When the cantilever reached the gold substrate, the repulsive force reached its upper limit, as indicated by the white line. The bulk of the substrate could not be penetrated by the cantilever tip and is therefore shown as a black area at the bottom of the image. The corresponding frequency change was obtained by averaging the values within the 100 nm width range and plotted against the *z*-distance from the substrate (Fig. 4F). As the *z*-position approached zero, the resonance frequency exponentially increased. The thickness of the repulsive layer (*Z*) was taken as the *z*-distance from the interface of the gold substrate to the point with a frequency change above 0 Hz and equaled 16 nm for the *gl*-PMEA/water interface. For the bare gold substrate, the repulsive layer was barely observed (Fig. S2B and S2C, ESI†). Therefore, the repulsive layer at the *gl*-PMEA/water interface was attributed to the presence of a hydrated PMEA layer. In contrast to *gl*-PMEA, *gc*-PMEA exhibited a notably thicker hydrated layer (Fig. 4G), which was manifested by a larger *Z* value of 37 nm (Fig. 4H).

The *gl*-PMEA and *gc*-PMEA interfaces exhibited different hydrated layer thicknesses despite having the same extended chain lengths. In particular, the chain length of *gl*-PMEA (M_n = 38 000) was calculated as ∼74 nm assuming a well-extended chain with an all-*trans* conformation and considerably exceeded

the corresponding *Z* value (16 nm). Thus, *gl*-PMEA was inferred to shrink and aggregate in the vicinity of the substrate, with the vertical thickness of the *gl*-PMEA layer accounting for 22% (= 100% × 16/74) of the length of the fully extended chain. At the employed grafting density (0.1 chains per nm²), the PMEA chains were easily entangled *via* hydrophobic interactions because of their mutual proximity (distance between neighboring chains = 3.2 nm). However, *gc*-PMEA formed a thicker repulsive layer (37 nm) than *gl*-PMEA despite having the same extended chain length. The former layer had a thickness corresponding to 50% of the extended chain length, indicating that *gc*-PMEA exhibited more stretched than *gl*-PMEA. This higher mobility was due to the decreased degree of entanglement caused by the looped nature of the *gc*-PMEA chains. Similarly, cyclic polymers were reported to exhibit less pronounced chain entanglement than linear polymers in an experimental study[63] and simulation study[64] on polymer viscosity. Although these studies targeted nongrafted polymers, the entanglement trend was the same as that observed for grafted chains. Both *gl*- and *gc*-PMEA layers absorbed water molecules, which resulted in polymer brush swelling. Subsequently, the less entangled chains of *gc*-PMEA diffused away from the substrate into bulk water, whereas this diffusion (and hence, swelling) was less pronounced for *gl*-PMEA because of its higher entanglement degree. Furthermore, irrespective of the topology of the grafted chains, the thinner swelling thickness compared to the stretched chain length is attributed to the water-insoluble properties of PMEA at the measured temperature of 23 °C.

The cell culture medium contains salts; therefore, FM-AFM observations were conducted in phosphate-buffered saline (PBS) to investigate the influence of salt on the swelling of *gl*-PMEA and *gc*-PMEA (details are provided in the ESI†). The repulsive layers were visualized on both interfaces (Fig. S3, ESI†). It was revealed that both types of PMEA swelled in PBS. The swelling thicknesses of 16 nm for the *gc*-PMEA was thicker than that of 13 nm for the *gl*-PMEA. This variation in the swelling behaviors including the hydration state may result in different bioresponses. Initial processes of hydration for *gc*- and *gl*-PMEA will be clarified in the next chapter.

Hydration water analysis of *gl*-PMEA and *gc*-PMEA by XES upon humidification

Given their principles, QCM measurements and FM-AFM observations are not sufficient to discuss the details of the water adsorbed on the *gl*-PMEA and *gc*-PMEA interfaces, *e.g.*, the interactions between the adsorbed water molecules and other water molecules or functional groups. Therefore, the electronic state of water molecules in wet materials was probed by XES.[54,65–67] Irradiation with soft X-rays excites inner-shell electrons to generate an intermediate state with a hole in the inner-shell orbital. This unstable state decays *via* the relaxation of valence electrons to inner-shell holes, and the excess energy is emitted as soft X-rays.[67] XES is a photon-in-photon-out (and hence, bulk-sensitive) technique that can be applied to wet samples under atmospheric pressure if an X-ray transmission window is used.[54,65,66] In particular, the oxygen K-edge XES

profiles of water molecules can be used to measure differences in hydrogen bonding.[68,69] Herein, we used XES to reveal the electronic structure of water molecules adsorbed on the *gl*-PMEA and *gc*-PMEA surfaces. By combining an atmosphere-controlled measurement cell with a precision humidification technique, we precisely adjusted the water content of the polymers and quantitatively characterized their initial hydration behavior. Previously, we used XES to reveal marked differences between the hydration states of blood-compatible and -incompatible polymers.[65] Herein, the excitation energy was set to 550 eV, which is well above the K-edge of oxygen, and the integrated intensity of the XES signal was therefore proportional to the number of oxygen atoms in the observed region. Water content was calculated from the difference in the integrated intensity of the XES spectra of dried and humidified polymers.

As XES does not distinguish between polymer and water oxygens, we extracted the water spectrum by subtracting the spectrum of dried PMEA from that of humidified PMEA. The shape of the adsorbed water spectrum was different from that of the bulk water spectrum, which suggested that the interactions between bulk water molecules differed from those between the water molecules near the *gl*- and *gc*-PMEA surfaces (Fig. 5A). The XES peaks of water were assigned to the $1b_2$ (O–H Sigma bond), $3a_1$ (H–O–H-linking bonding), and $1b_1$ (nonbonding lone pair) orbitals from the low-energy side.[67] Although the results of XES may resemble those of high-resolution photoelectron spectroscopy,[70] XES profiles often have shapes different from those of photoelectron spectra because of the involvement of core-excited intermediate states in the former case.[71–73] The XES profile of bulk water in Fig. 5A is a typical example. The $1b_1$ orbital of bulk water was represented by a single peak in the corresponding photoelectron spectrum, whereas two peaks were observed in the related XES profile.[68,70,74–76] Although its origin is debatable, this splitting is thought to reflect the differences in hydrogen bonding between water molecules.[69,71,72,77] Previously, we combined XES and humidified AFM observations to show that the interaction of adsorbed water in the primary hydration shell of the scaffold is important for IW formation.[54]

To quantitatively evaluate the dependence of the XES profiles on water content, we fitted three or four peaks (Fig. S4, ESI†), revealing that the $1b_1$ peak energy ranged from 526.85 to 527.1 eV. The low-energy side of the $1b_1$ peak (designated as $1b_1{}'$) originated from hydrogen-bonded tetrahedrally coordinated water molecules and appeared at 525.9 eV, whereas the high-energy side ($1b_1{}''$) originated from distorted hydrogen-bonded water molecules and appeared at 526.8 eV.[68,69] *gl*-PMEA and *gc*-PMEA showed a difference in the dependence of the $1b_1$ peak energy of hydration water on water content (Fig. 5A). For *gc*-PMEA, the $1b_1$ peak energy increased with increasing water content, whereas the reverse was true for *gl*-PMEA (Fig. 5B). This implied that in the low-water-content region, hydrogen bonds and interactions between water molecules developed in the vicinity of *gl*-PMEA but not *gc*-PMEA.

Previous DSC analyses of *gl*-PMEA and *gc*-PMEA showed that the latter polymer was more conducive to NFW and IW formation than the former.[56] These results need to be considered with care, as DSC analysis provides information on the average
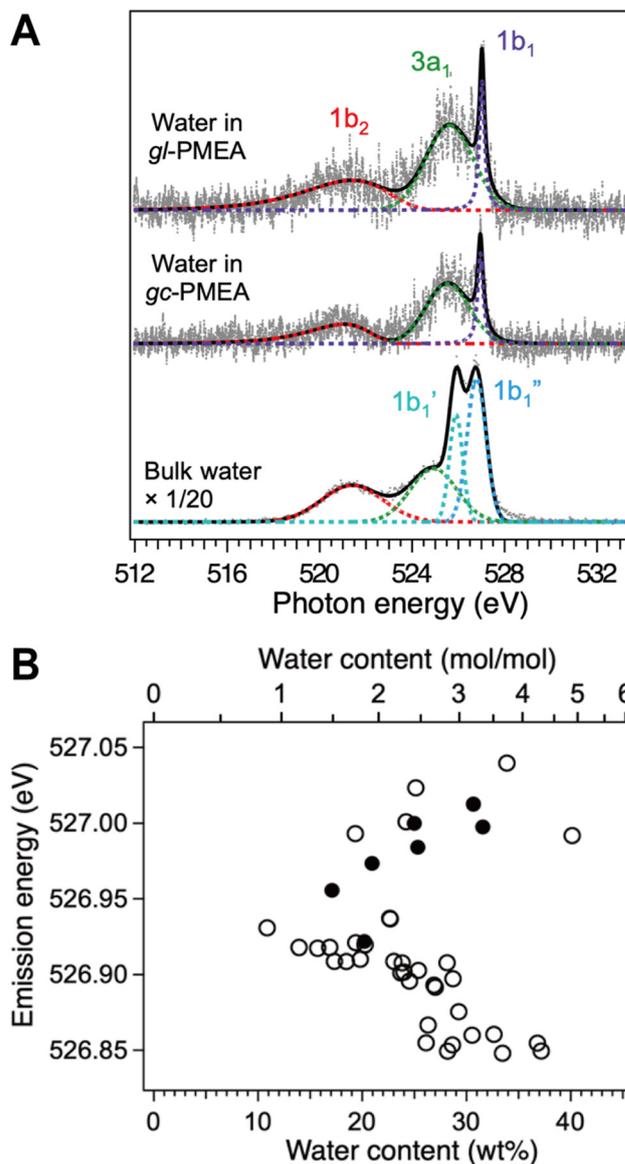

Fig. 5 (A) X-ray emission spectra of 60%RH humidified *gl*-PMEA, 50%RH humidified *gc*-PMEA, and bulk water. The spectrum of adsorbed water was obtained as the difference between the spectra of humidified and dried polymers. (B) Energy of the $1b_1$ peak of water molecules adsorbed on *gl*-PMEA (open circles) and *gc*-PMEA (filled circles) as a function of water content.

hydration state of the whole polymer matrix and not only for the outermost surface. Assuming that the bonding state of the primary hydration shell of the polymer depends only on its functional groups, the water (NFW) contents and biocompatibilities of *gl*-PMEA and *gc*-PMEA should be identical. Given that these polymers have the same primary structure and force field sensed by the water molecules in the primary hydration shell, they should exhibit identical binding states to the primary hydration shell. In other words, this set of results means that the interaction of the polymer primary hydration shell is affected by polymer primary and secondary structures.

Fig. 5B shows the interactions of water molecules at water contents of 10–40 wt%. The equilibrium water content of bulk polymers is commonly measured using DSC. For example, the equilibrium water content of *l*-PMEA was reported as 9 wt%.[78] Such standardized measurements are important for facilitating material comparison and promoting industrial applications. However, in works on the water–polymer interface, such as the present study, the equilibrium water content measured by standard methods should be used with great care. For example, the equilibrium water content at the top surface of *l*-PMEA was measured by neutron reflectometry as ≥ 50 wt%.[52] As the *l*- and *c*-PMEAs in the present study were directly grafted onto the SiC/Au substrate to afford a perfect water–polymer interface, the overall water content possibly exceeded 50 wt%. Therefore, the range in Fig. 5B is not indicative of overhydration with respect to the PMEAs. This range was converted into the number of water molecules adsorbed per MEA side chain (0.9–4.8 mol mol^{-1}). In other words, Fig. 5B shows the early to midstage development of water adsorption on the PMEAs. There is a possibility that the presence of separate data points in XES of *gl*-PMEA shifting to higher energy are due to presence of gaseous water signals dominated at pinholes in the Au layer potentially resulting from lot-to-lot variations in the SiC/Au substrate. The FM-AFM observations and QCM measurements were useful for investigating the effect of the secondary polymer structure on the hydration state. The QCM measurements showed that both *gl*-and *gc*-PMEA chains hydrate in water. The 1-octanol/water partition coefficient of PMEA ($\log P_{OW} = -0.76$[79,80]) suggests that PMEA is slightly more hydrophilic and elongation in water is energetically favorable. However, the thickness of the repulsive layer in the fully hydrated state was notably greater for *gc*-PMEA than for *gl*-PMEA. From these facts, we concluded that *gc*-PMEA elongates strongly in water, whereas *gl*-PMEA weakly. The entanglement of the *gl*-PMEA chains was ascribed to the average interchain distance being short relative to the elongated chain length. Previous studies suggested that *l*-PMEA chains form a head-to-tail (H-to-T) stacked structure with the carbonyl and methylene groups of proximal side chains, even in the dry state.[81] However, hydrogen bonds are not involved in side-chain entanglement in the dry state. Molecular dynamics simulations demonstrated that H-to-T stacked PMEA forms hydrogen bonds in the low-water-content state, with water molecules bridging the side-chain carbonyl and methylene groups.[82] *gl*-PMEA did not sufficiently swell when immersed in water, which suggested that the H-to-T stacked structure was maintained even at a saturated water content. In other words, in the H-to-T stacked structure, the hydrophilic groups of *l*-PMEA were shielded, and hydration by water molecules bound to the hydrophilic groups as scaffolds was suppressed. However, as both ends of *gc*-PMEA were fixed, H-to-T stacks were less likely to form between the side chains, and water molecules could approach the hydrophilic groups without being blocked. Therefore, we ascribed the lower platelet adhesion of *c*-PMEA to the ample formation of IW due to the unrestricted access of water molecules to hydrophilic groups.

Although PMEA was grafted onto a gold substrate, the average chain-to-chain distance of *gl*-PMEA was sufficiently small compared with the elongated chain length, and the side chains were assumed to form an H-to-T stacked structure. Therefore, the results of previous studies on bulk *l*-PMEA are applicable to the present study.

The hydration state, especially the presence of IW, was reported to affect the affinity between polymers and cells.[34–36] Given that tumor cells have a greater preference for IW-rich polymers than normal cells, the difference in the bioresponses of *gl*-PMEA and *gc*-PMEA was ascribed to IW formation. Elastic moduli and topologies are often used to rationalize biological phenomena, such as cell adhesion, proliferation, and differentiation, although these factors are often insufficient to elucidate the mechanism at the molecular scale. Herein, FM-AFM imaging in water visualized the polymer swelling state. QCM demonstrated the hydration of the polymer based on mechanical oscillation motion. To further discuss the molecular interpretation of the hydration state, we attempted to observe it using XES at a controlled water content. The reduced bioresponsiveness of *l*-PMEA was ascribed to the shielding of its hydrophilic groups due to side-chain entanglement, which inhibited IW formation. In other words, to control bioresponsiveness, one should control the hydration state of the functional groups.

Given that polymer functions are expressed by the interactions between molecules and polymer chains near the interface, measurements focusing on the interface vicinity are important for clarifying the origin of these functions. The polymer–water interface is at least several nanometers to tens of nanometers wide, as shown by our FM-AFM results. Few studies have performed electronic structure measurements focusing on interfaces with no clear boundaries. Herein, the difficulty of characterizing the interfacial electronic structure of wet samples was overcome using a combination of equal-length grafted polymer chains (polymer brushes), precise humidification control, and XES. The combination of FM-AFM, QCM, and XES allowed observation under wet conditions and was concluded to be a powerful tool for understanding the polymer–water interface and functional expression mechanism of polymers.

Methods

No unexpected or unusually high safety hazards were encountered.

Preparation of polymer-grafted surfaces

Polymer-grafted surfaces were prepared as described elsewhere.[54] Thiol-terminated *l*-PMEA and disulfide bond–containing *c*-PMEA were dissolved in methanol to an arbitrary concentration. The gold substrate was treated with these solutions, washed with the same solvent, and dried *in vacuo* for 3 h at 30 °C. Polymer brush density (σ) was calculated from the modification-induced frequency change determined by QCM measurements. The conditions used for the fabrication of polymer brushes and their characteristics are summarized in Table S1 (ESI†).

Human platelet adhesion test

Human platelets were obtained from whole blood samples purchased from the Japanese Red Cross Society (Japan). The corresponding adhesion test was performed within three days of whole blood collection. The related details are provided in the ESI.†

Cell adhesion experiments

NHDF and MDA-MB-231 cells were purchased from Lonza (USA) and the American Type Culture Collection (USA), respectively. HeLa, MCF-7, and HepG2 cells were purchased from the Cell Resource Center for Biomedical Research at the Institute of Development, Aging, and Cancer (Tohoku University, Japan). The cells were cultured in Dulbecco's Modified Eagle Medium (Gibco, Thermo Fisher Scientific Inc., USA) containing 10% fetal bovine serum (BioWest, Funakoshi Co., Ltd, Japan) and 1% penicillin streptomycin (Gibco, Thermo Fisher Scientific Inc., USA). Further experimental details are provided in the ESI.†

AFM characterization of polymer-grafted surfaces

The xy-dimensional height images and force mapping images were obtained for the horizontal planes of the gl-PMEA and gc-PMEA surfaces in deionized water at room temperature (25 °C) using PFT-mode AFM (BioScope Resolve, Bruker). FM-AFM (SPM-8100FM, Shimadzu Co.) was used to acquire surface-normal cross-sectional images in water at 23 °C. Further experimental details are provided in the ESI.†

QCM-based quantitation of grafting density and hydration water

The grafting densities and hydration water amounts of gl-PMEA and gc-PMEA were measured using QCM methods similar to those used previously.[53,61] Further experimental details are provided in the ESI.†

XES analyses of polymer-grafted surfaces under controlled-humidity conditions

XES measurements were performed using an ultra-high-resolution soft X-ray emission spectrometer at the Spring-8 BL07LSU HORNET station[83,84] for c-PMEA and l-PMEA grafted onto a SiC (150 nm)/Au (11 nm) substrate (NTT Advanced Technology Co.) at a density of 0.1 chains per nm^2 and 0.05 chains per nm^2, respectively. The excitation energy (550 eV) exceeded the O 1s core absorption threshold, thus enabling the ionization of water molecules and analysis of the O 2p partial density of states in the occupied valence orbitals. Further experimental details are provided in the ESI.†

Conclusions

Herein, we prepared model surfaces composed of l- and c-PMEAs (gl-PMEA and gc-PMEA, respectively) with different hydration states and analyzed them by QCM, FM-AFM, and XES under wet conditions to probe the relationship between bioresponsivity and hydration water. Both surfaces suppressed the adhesion of human platelets but differed in the adhesion behaviors of normal and tumor cells despite having the same areal density of MEA units,

which suggested that bioresponsiveness was affected by the hydration state. QCM measurements indicated that PMEA interacts with surrounding water. FM-AFM measurements revealed a thicker swelling surface for gc-PMEA because of its less entangled cyclic structure. To rationalize the differences in the surface hydration states, we performed XES measurements by controlling the amount of hydration water under humid conditions. In the low-water-content region, hydrogen bonds or interactions between water molecules developed in the vicinity of gl-PMEA but not gc-PMEA. Thus, the initial hydration behavior of the gc-PMEA surface, which promoted IW formation, was different from that of the gl-PMEA surface. Based on these results, we concluded that the gl-PMEA surface exhibited a lower bioresponsiveness than the gc-PMEA surface because of the shielding of hydrophilic groups due to side-chain entanglement in the former case and its inhibitory effect on IW formation. The combined results suggest that the adjustment and optimization of the amount of IW on outermost biomaterial surfaces enable the control of bioresponses, including the selective isolation of tumor cells.

Author contributions

M. T. and Y. H. conceived the research. S. N., N. K., and S. S. designed and performed the experiments. M. T. and Y. H. obtained funding for the project. M. T. and Y. H. supervised the research. S. N., N. K., S. S., Y. H., and M. T. co-wrote and edited the manuscript. All authors discussed the results and commented on the manuscript.

Data availability

All data supporting the findings of this study are presented in the article and ESI.† Additional data are available from the corresponding author upon reasonable request.

Conflicts of interest

There are no conflicts to declare.

Acknowledgements

Notes and references

1 R. Langer and J. P. Vacanti, *Science*, 1993, **260**, 920–926.

2 Y. Haraguchi, T. Shimizu, M. Yamato and T. Okano, *Stem Cells Transl. Med.*, 2012, **1**, 136–141.

3 G. L. Koons, M. Diba and A. G. Mikos, *Nat. Rev. Mater.*, 2020, **5**, 584–603.

4 Y. Zhao, S. Song, X. Ren, J. Zhang, Q. Lin and Y. Zhao, *Chem. Rev.*, 2022, **122**, 5604–5640.

5 M. C. Catoira, L. Fusaro, D. Di Francesco, M. Ramella and F. Boccafoschi, *J. Mater. Sci.: Mater. Med.*, 2019, **30**, 115.

6 S. Nishimura, T. Yoshida, N. Higashi and T. Koga, *Adv. Mater. Technol.*, 2024, **9**, 2301598.

7 D. Schmaljohann, *Adv. Drug. Delivery Rev.*, 2006, **58**, 1655–1670.

8 E. Gil and S. Hudson, *Prog. Polym. Sci.*, 2004, **29**, 1173–1222.

9 H. Suhara, Y. Sawa, M. Nishimura, H. Oshiyama, K. Yokoyama, N. Saito and H. Matsuda, *Ann. Thorac. Surg.*, 2001, **71**, 1603–1608.

10 S. Nishimura, T. Ueda, S. Kobayashi and M. Tanaka, *ACS Appl. Polym. Mater.*, 2020, **2**, 4790–4801.

11 D. Baykut, F. Bernet, J. Wehrle, K. Weichelt, P. Schwartz and H. R. Zerkowski, *Eur. J. Med. Res.*, 2001, **6**, 297–305.

12 S. Nishimura, N. Hokazono, Y. Taki, H. Motoda, Y. Morita, K. Yamamoto, N. Higashi and T. Koga, *ACS Appl. Mater. Interfaces*, 2019, **11**, 24577–24587.

13 M. Tanaka, S. Kobayashi, D. Murakami, F. Aratsu, A. Kashiwazaki, T. Hoshiba and K. Fukushima, *Bull. Chem. Soc. Jpn.*, 2019, **92**, 2043–2057.

14 S. Nishimura and M. Tanaka, *Bull. Chem. Soc. Jpn.*, 2023, **96**, 1052–1070.

15 D. D. Deligianni, N. D. Katsala, P. G. Koutsoukos and Y. F. Missirlis, *Biomaterials*, 2000, **22**, 87–96.

16 J. Y. Martin, Z. Schwartz, T. W. Hummert, D. M. Schraub, J. Simpson, J. Lankford Jr., D. D. Dean, D. L. Cochran and B. D. Boyan, *J. Biomed. Mater. Res.*, 1995, **29**, 389–401.

17 N. M. Alves, I. Pashkuleva, R. L. Reis and J. F. Mano, *Small*, 2010, **6**, 2208–2220.

18 C. Xu, F. Yang, S. Wang and S. N. Ramakrishna, *J. Biomed. Mater. Res. A*, 2004, **71A**, 154–161.

19 G. R. Owen, J. Jackson, B. Chehroudi, H. Burt and D. M. Brunette, *Biomaterials*, 2005, **26**, 7447–7456.

20 M. Padial-Molina, P. Galindo-Moreno, J. E. Fernández-Barbero, F. O'Valle, A. B. Jódar-Reyes, J. L. Ortega-Vinuesa and P. J. Ramón-Torregrosa, *Acta Biomater.*, 2011, **7**, 771–778.

21 R. Tzoneva, N. Faucheux and T. Groth, *Biochim. Biophys. Acta, Gen. Subj.*, 1770, **2007**, 1538–1547.

22 T. G. van Kooten, J. M. Schakenraad, H. C. van der Mei and H. J. Busscher, *Biomaterials*, 1992, **13**, 897–904.

23 R. A. Gittens, L. Scheideler, F. Rupp, S. L. Hyzy, J. Geis-Gerstorfer, Z. Schwartz and B. D. Boyan, *Acta Biomater.*, 2014, **10**, 2907–2918.

24 T. Yeung, P. C. Georges, L. A. Flanagan, B. Marg, M. Ortiz, M. Funaki, N. Zahir, W. Ming, V. Weaver and P. A. Janmey, *Cell Motil. Cytoskeleton*, 2005, **60**, 24–34.

25 A. J. Engler, S. Sen, H. L. Sweeney and D. E. Discher, *Cell*, 2006, **126**, 677–689.

26 S. Nemir, H. N. Hayenga and J. L. West, *Biotechnol. Bioeng.*, 2010, **105**, 636–644.

27 R. H. Schmedlen, K. S. Masters and J. L. West, *Biomaterials*, 2002, **23**, 4325–4332.

28 A. Banerjee, M. Arha, S. Choudhary, R. S. Ashton, S. R. Bhatia, D. V. Schaffer and R. S. Kane, *Biomaterials*, 2009, **30**, 4695–4699.

29 H. Y. Yoshikawa, F. F. Rossetti, S. Kaufmann, T. Kaindl, J. Madsen, U. Engel, A. L. Lewis, S. P. Armes and M. Tanaka, *J. Am. Chem. Soc.*, 2011, **133**, 1367–1374.

30 J. Thiele, Y. Ma, S. M. C. Bruekers, S. Ma and W. T. S. Huck, *Adv. Mater.*, 2014, **26**, 125–148.

31 P. Kumar, S. Han and H. E. Stanley, *J. Phys.: Condens. Matter*, 2009, **21**, 504108.

32 M. Tanaka, T. Motomura, N. Ishii, K. Shimura, M. Onishi, A. Mochizuki and T. Hatakeyama, *Polym. Int.*, 2000, **49**, 1709–1713.

33 M. Tanaka, T. Motomura, M. Kawada, T. Anzai, Y. Kasori, T. Shiroya, K. Shimura, M. Onishi and A. Mochizuki, *Biomaterials*, 2000, **21**, 1471–1481.

34 T. Hoshiba, M. Nikaido and M. Tanaka, *Adv. Healthcare Mater.*, 2014, **3**, 775–784.

35 T. Hoshiba, E. Nemoto, K. Sato, T. Orui, T. Otaki, A. Yoshihiro and M. Tanaka, *PLoS One*, 2015, **10**, e0136066.

36 T. Hoshiba, E. Nemoto, K. Sato, H. Maruyama, C. Endo and M. Tanaka, *Biomacromolecules*, 2016, **17**, 3808–3815.

37 T. Hoshiba, T. Otaki, E. Nemoto, H. Maruyama and M. Tanaka, *ACS Appl. Mater. Interfaces*, 2015, **7**, 18096–18103.

38 K. Sato, S. Kobayashi, M. Kusakari, S. Watahiki, M. Oikawa, T. Hoshiba and M. Tanaka, *Macromol. Biosci.*, 2015, **15**, 1296–1303.

39 K. Sato, S. Kobayashi, A. Sekishita, M. Wakui and M. Tanaka, *Biomacromolecules*, 2017, **18**, 1609–1616.

40 S. Kobayashi, M. Wakui, Y. Iwata and M. Tanaka, *Biomacromolecules*, 2017, **18**, 4214–4223.

41 T. Sonoda, S. Kobayashi, K. Herai and M. Tanaka, *Macromolecules*, 2020, **53**, 8570–8580.

42 C. Sato, M. Aoki and M. Tanaka, *Colloids Surf., B*, 2016, **145**, 586–596.

43 K. Nishida, T. Anada, S. Kobayashi, T. Ueda and M. Tanaka, *Acta Biomater.*, 2021, **134**, 313–324.

44 K. Nishida, S. Sekida, T. Anada and M. Tanaka, *ACS Biomater. Sci. Eng.*, 2022, **8**, 672–681.

45 K. Nishida, T. Anada and M. Tanaka, *Adv. Drug. Delivery Rev.*, 2022, **186**, 114310.

46 T. Hatakeyama, M. Tanaka and H. Hatakeyama, *J. Biomater. Sci., Polym. Ed.*, 2010, **21**, 1865–1875.

47 T. Hatakeyama, M. Tanaka and H. Hatakeyama, *Acta Biomater.*, 2010, **6**, 2077–2082.

48 A. Mochizuki, T. Hatakeyama, Y. Tomono and M. Tanaka, *J. Biomater. Sci., Polym. Ed.*, 2009, **20**, 591–603.

49 S. Morita, M. Tanaka and Y. Ozaki, *Langmuir*, 2007, **23**, 3750–3761.

50 Y. Ikemoto, Y. Harada, M. Tanaka, S. Nishimura, D. Murakami, N. Kurahashi, T. Moriwaki, K. Yamazoe, H. Washizu, Y. Ishii and H. Torii, *J. Phys. Chem. B*, 2022, **126**, 4143–4151.

51 Y. Miwa, H. Ishida, M. Tanaka and A. Mochizuki, *J. Biomater. Sci., Polym. Ed.*, 2010, **21**, 1911–1924.

52 T. Hirata, H. Matsuno, M. Tanaka and K. Tanaka, *Phys. Chem. Chem. Phys.*, 2011, **13**, 4928–4934.

53 T. Ueda, D. Murakami and M. Tanaka, *J. Polym. Sci.*, 2021, **59**, 2763–2770.

54 D. Murakami, K. Yamazoe, S. Nishimura, N. Kurahashi, T. Ueda, J. Miyawaki, Y. Ikemoto, M. Tanaka and Y. Harada, *Langmuir*, 2022, **38**, 1090–1098.

55 D. Murakami, S. Nishimura, Y. Tanaka and M. Tanaka, *Biomater. Adv.*, 2022, **133**, 112596.

56 S. Nishimura, T. Ueda, D. Murakami and M. Tanaka, *Org. Mater.*, 2021, **3**, 214–220.

57 L. L. Rouhana, M. D. Moussallem and J. B. Schlenoff, *J. Am. Chem. Soc.*, 2011, **133**, 16080–16091.

58 Y. Ikada, Blood-compatible polymers, in *Polymers in medicine*, ed. K. Dusek, Springer-Verlag Berlin, Heidelberg, 1984, pp. 103–140.

59 E. Shin, C. T. Lim, U. J. Kang, M. Kim, J. Park, D. Kim, W. Choi, J. Hong, C. Baig, D. W. Lee and B.-S. Kim, *Macromolecules*, 2020, **53**, 3551–3562.

60 T. Hirata, H. Matsuno, D. Kawaguchi, M. Inutsuka, T. Hirai, M. Tanaka and K. Tanaka, *Phys. Chem. Chem. Phys.*, 2017, **19**, 1389–1394.

61 T. Ozeki, M. Morita, H. Yoshimine, H. Furusawa and Y. Okahata, *Anal. Chem.*, 2007, **79**, 79–88.

62 H. Furusawa, T. Ozeki, M. Morita and Y. Okahata, *Anal. Chem.*, 2009, **81**, 2268–2273.

63 R. Pasquino, T. C. Vasilakopoulos, Y. C. Jeong, H. Lee, S. Rogers, G. Sakellariou, J. Allgaier, A. Takano, A. R. Brás, T. Chang, S. Gooßen, W. Pyckhout-Hintzen, A. Wischnewski, N. Hadjichristidis, D. Richter, M. Rubinstein and D. Vlassopoulos, *ACS Macro Lett.*, 2013, **2**, 874–878.

64 G. Subramanian and S. Shanbhag, *Phys. Rev. E*, 2008, **77**, 011801.

65 K. Yamazoe, Y. Higaki, Y. Inutsuka, J. Miyawaki, Y.-T. Cui, A. Takahara and Y. Harada, *Langmuir*, 2017, **33**, 3954–3959.

66 R. Watanabe, T. Sakamoto, K. Yamazoe, J. Miyawaki, T. Kato and Y. Harada, *Angew. Chem., Int. Ed.*, 2020, **59**, 23461–23465.

67 T. Fransson, Y. Harada, N. Kosugi, N. A. Besley, B. Winter, J. J. Rehr, L. G. M. Pettersson and A. Nilsson, *Chem. Rev.*, 2016, **116**, 7551–7569.

68 T. Tokushima, Y. Harada, O. Takahashi, Y. Senba, H. Ohashi, L. G. M. Pettersson, A. Nilsson and S. Shin, *Chem. Phys. Lett.*, 2008, **460**, 387–400.

69 T. Tokushima, Y. Harada, Y. Horikawa, O. Takahashi, Y. Senba, H. Ohashi, L. G. M. Pettersson, A. Nilsson and S. Shin, *J. Electron Spectrosc. Relat. Phenom.*, 2010, **177**, 192–205.

70 K. Nishizawa, N. Kurahashi, K. Sekiguchi, T. Mizuno, Y. Ogi, T. Horio, M. Oura, N. Kosugi and T. Suzuki, *Phys. Chem. Chem. Phys.*, 2011, **13**, 413–417.

71 O. Takahashi, R. Yamamura, T. Tokushima and Y. Harada, *Phys. Rev. Lett.*, 2022, **128**, 086002.

72 O. Takahashi and L. G. M. Pettersson, *Mol. Phys.*, 2023, **121**, e2170686.

73 V. Savchenko, M. Odelius, A. Banerjee, N. Ignatova, A. Föhlisch, F. Gelmukhanov and V. Kimberg, *J. Chem. Phys.*, 2023, 159.

74 B. Winter and M. Faubel, *Chem. Rev.*, 2006, **106**, 1176–1211.

75 N. Kurahashi, S. Karashima, Y. Tang, T. Horio, B. Abulimiti, Y.-I. Suzuki, Y. Ogi, M. Oura and T. Suzuki, *J. Chem. Phys.*, 2014, 140.

76 K. M. Lange, R. Könnecke, M. Soldatov, R. Golnak, J.-E. Rubensson, A. Soldatov and E. F. Aziz, *Angew. Chem., Int. Ed.*, 2011, **50**, 10621–10625.

77 J. A. Sellberg, T. A. McQueen, H. Laksmono, S. Schreck, M. Beye, D. P. DePonte, B. Kennedy, D. Nordlund, R. G. Sierra, D. Schlesinger, T. Tokushima, I. Zhovtobriukh, S. Eckert, V. H. Segtnan, H. Ogasawara, K. Kubicek, S. Techert, U. Bergmann, G. L. Dakovski, W. F. Schlotter, Y. Harada, M. J. Bogan, P. Wernet, A. Föhlisch, L. G. M. Pettersson and A. Nilsson, *J. Chem. Phys.*, 2015, **142**, 044505.

78 M. Tanaka and A. Mochizuki, *J. Biomed. Mater. Res. A*, 2004, **68A**, 684–695.

79 S. Nishimura, K. Nishida, S. Shiomoto and M. Tanaka, *Mater. Adv.*, 2022, **3**, 5043–5054.

80 K. Nishida, S. Nishimura and M. Tanaka, *Biomacromolecules*, 2022, **23**, 1569–1580.

81 A. Shabbir, I. Javakhishvili, S. Cerveny, S. Hvilsted, A. L. Skov, O. Hassager and N. J. Alvarez, *Macromolecules*, 2016, **49**, 3899–3910.

82 N. Yasoshima, T. Ishiyama, M. Gemmei-Ide and N. Matubayasi, *J. Phys. Chem. B*, 2021, **125**, 12095–12103.

83 S. Yamamoto, Y. Senba, T. Tanaka, H. Ohashi, T. Hirono, H. Kimura, M. Fujisawa, J. Miyawaki, A. Harasawa, T. Seike, S. Takahashi, N. Nariyama, T. Matsushita, M. Takeuchi, T. Ohata, Y. Furukawa, K. Takeshita, S. Goto, Y. Harada, S. Shin, H. Kitamura, A. Kakizaki, M. Oshima and I. Matsuda, *J. Synchrotron Radiat.*, 2014, **21**, 352–365.

84 Y. Harada, M. Kobayashi, H. Niwa, Y. Senba, H. Ohashi, T. Tokushima, Y. Horikawa, S. Shin and M. Oshima, *Rev. Sci. Instrum.*, 2012, **83**, 013116.